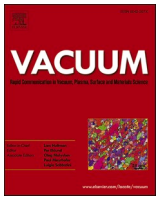
Vacuum 233 (2025) 113964



Contents lists available at ScienceDirect

Vacuum

journal homepage: www.elsevier.com/locate/vacuum





Characterization of particles inside the metal vapor plume during laser beam welding in atmosphere and vacuum

Christian Frey [a,*], Johannes Wahl [b], Kathrin Schmidt [a], Simon Olschok [a], Christian Hagenlocher [b], Thomas E. Weirich [c], Thomas Graf [b], Uwe Reisgen [a]

[a] RWTH Aachen University, Welding and Joining Institute, Pontstrasse 49, D-52062, Aachen, Germany
[b] University of Stuttgart, Institut für Strahlwerkzeuge, Pfaffenwaldring 43, D-70569, Stuttgart, Germany
[c] RWTH Aachen University, Central Facility for Electron Microscopy (GFE), Ahornstrasse 55, D-52074, Aachen, Germany

ARTICLE INFO

Handling Editor: Prof. L.G. Hultman

Keywords:
Laser beam welding under vacuum (LaVa)
Stainless steel
Metal vapor plume
Nanoparticles
Scattering
Multi-wavelength-methode

ABSTRACT

During laser beam welding of metals, process emissions are generated above the workpiece surface, through which the incident laser beam passes. One part of the process emissions are particles which arise from the hot metal vapor phase and agglomerate to form larger chains until they have cooled down completely. Depending on the chemical composition and size of this material emissions, the light waves are reflected, absorbed or scattered to varying degrees. The Mie theory comprehensively describes the scattering and absorption behavior of particles and essentially covers the welding plume produced during laser beam welding with a few assumptions. To specify these assumtions in more detail, this study analyzes the nanoparticles deposited on a glass carrier in the beam path of the laser. The deposition shows prismatic and octahedral structures in the scanning electron microscope, besides the predominantly spherical particles. In a vacuum and therefore with a reduced oxygen content, the ammount of emissions of the keyhole decreases and particles collected in the plume are identified as solid solution bcc-type particles containing Cr, Cu, Fe, Mn, and Ni. In atmosphere at 1000 mbar however, complex solid solutions phases with diffraction patterns compatible to spinel-type $NiCr_2O_4$ and $NiFe_2O_4$ are formed.

1. Introduction

Laser beam welding under vacuum goes back to 1980′s with the aim to suppress the generated plasma plume during laser deep penetration welding with a CO_2 laser [1]. Since then, research drive to utilize the beneficial effect of the vacuum such as deeper weld seams [2]. During deep penetration welding with solid-state lasers, the so-called metal vapor plume forms above the welding process due to the vaporization of the workpiece. This is accompanied by electromagnetic and material emissions [3], as well as acoustic emissions [4]. While the acoustic and electromagnetic radiation is often used for process monitoring, the material emission is perceived as disturbing, as it contributes significantly to the extinction of solid-state laser and consequently to process instabilities [5]. The extinction of the laser beam depends mainly on the particle formation inside the metal vapor plume. This should not be equated with the plasma absorption by welding with a CO_2 laser, which depends on the electron temperature [6]. The temperatures of the escaping metal vapor depends, among shielding gas and material, on the used laser wavelength. When welding steel with a solid-state laser (λ~1064 nm), the temperature of the metal vapor at the opening of the capillary rises up to 4000 K [7] while using CO_2 lasers heats the plume up to 7300 K [8]. Consequently, when welding with a solid-state lasers, no plasma is produced, only weak ionized metal vapor which causes less than 1 % absorption of the laser radiation [9]. The metal vapor plume in laser beam welding with solid-state lasers on atmosphere is characterized by three zones [10]. Zone 1 directly above the capillary is dominated by thermal radiation, which can be attributed to the hot metal vapor. Around 100 mm above the process, in zone 3, the scattered laser light dominates, which is caused by particles in the beam path. In the second zone, a superposition of scattered laser light and thermal radiation occurs, which is characterized by hot metal vapor, reheated particles and Mie scattering of the processing laser on condensed and agglomerated particles. Within the metal vapor plume, this phase transformation from vaporous to liquid state does not occur uniformly due to the random density distribution, but rather as a dynamic process based on collisions of particles with each other. The formation of the

* Corresponding author.
E-mail address: frey@isf.rwth-aachen.de (C. Frey).

https://doi.org/10.1016/j.vacuum.2024.113964
Received 25 October 2024; Received in revised form 17 December 2024; Accepted 17 December 2024
Available online 18 December 2024
0042-207X/© 2024 The Authors. Published by Elsevier Ltd. This is an open access article under the CC BY license (http://creativecommons.org/licenses/by/4.0/).

resulting particle collective in the metal vapor plume is based on a preceding nucleation process, whereby a distinction is made between homogeneous and heterogeneous nucleation [5]. Homogeneous nucleation takes place by collision and union of particles with each other, but for this to occur, a sufficient number of particles must be present, i.e. the metal vapor must be in a supersaturated state. Heterogeneous nucleation does not require supersaturation because condensation takes place on existing surfaces (e.g. foreign particles). Based on these two mechanisms, the particles are formed in the metal vapor plume, whereby the condensation rate decreases sharply with increasing distance from the workpiece surface, so that the resulting particle size distribution is largely formed close to the surface [11]. In more distant areas of the metal vapor plume, the particles interact with each other by collision and agglomerate to form larger structures known as clusters [12]. The interaction between the laser beam and the particles or particle clusters is reflected in a reduction in the welding depth of up to 20 % depending on the application [13]. In addition to the inclination and the dynamic behavior of the metal vapor plume, the selected process parameters also determine the evaporation rate and thus the extent of the interaction between the laser and the metal vapor [14]. The reduction in welding depth is more pronounced at wavelengths in the visible range (515 nm), which are used for joining copper. The use of a shielding gas alone, which blows away the metal vapor plume, results in a 67 % increase in welding depth [15].

Mie theory, which was first published by Gustav Mie in 1908, can be used to calculate the extinction of electromagnetic radiation with a wavelength λ on spherical particles with an arbitrary radius and a complex refractive index n_p [16]. Mie theory is based on the solution of Maxwell's equations for the scattering of a plane electromagnetic wave by a particle. The extinction fraction is distributed differently depending on the material, ambient medium, particle size and wavelength. The multi-wavelength method is used to investigate the particle size in the metal vapor plume during laser beam welding. The size of the particles lies in the size range of the applied wavelength, the so-called Mie range [17]. For the application of the multi-wavelength method, it is assumed that only spherical particles are present in the investigated medium and that there is no multiple scattering of the light beams on the particles. It is also assumed that the particle size distribution follows a normalized impulse function, which means that the values are to be evaluated as the average particle radius $\underline{r}$ [3].

Especially when welding steels, steel alloys or other materials with an affinity for oxygen, it is difficult to determine the composition of the particles in the metal vapor plume. In the literature, this is sometimes assumed differently or not clearly stated, which means that various particle size distributions can be found (iron [3,18], magnetite [13], not clear [19,20]). In addition, different atmospheric conditions can influence the particle size distribution as well. For example, without shielding gas, a particle size from approximately 50 nm can be detected for welds on low-alloy steels [3] and between 28 nm and 33 nm for stainless steels [5]. In argon or helium atmospheres, on the other hand, the average particle size is in the range of 10–30 nm, which can be reduced to the single-digit nano range with reduced working pressure [12]. In addition, when welding with reduced working pressure, it can be seen that the particle deposits take on a reddish color with a relatively high residual oxygen content of approx. 10 vol% in the argon atmosphere [21]. With decreasing residual oxygen content, a dark black coloration of the deposits is predominantly visible. According to the colors, the reddish deposit can be attributed to hematite, while the black deposit indicates magnetite [22]. In powder production, it is known that at normal pressure, maghemite γ-Fe_2O_3 is formed as the main component of the nanopowder from the vaporized starting material hematite α-Fe_2O_3 [23]. With increasing oxygen partial pressure in the condensation area, the proportion of polymorphs ε-Fe_2O_3 also increases. However, there is no investigation availble which analyses the exact composition and dependency on working pressure of the particles in the metal vapor plume during laser beam welding. The aim of this study is to determine the relation of particle size and composition within the propagation of the metal vapor plume to gain a deeper understanding of the realistic attenuation of the laser beam. The results will also serve as basis for assumptions for the multi-wavelength method and process simulations.

2. Experimental procedure

The LaVa L-95 laser beam welding system from FOCUS is used for the tests, which enables welding from atmospheric pressure to 0.1 mbar. The TruDisk 16,002 disk laser from TRUMPF with a wavelength of 1030 nm and maximum power of 16,000 W serves as the laser beam source. The laser soruce is connected to the IPG D50 scanner optic from IPG via a 200 µm optical fiber and measures a beam parameter product of 8.4 mm*mrad at 6000 W laser power for this setup. The 200 mm collimation length and 400 mm focusing length generate a focus diameter of 384 µm in the focal plane, as shown for the beam measurement carried out in Fig. 1 a).

To collect the particles, a holder with a cleaned glass carrier is placed over the welding position through which the laser beam passes on the way to the sample, see Fig. 1 b). The glass carrier is a commercially available protective glass for laser optics, which is explicitly intended for the wavelength of 1030 nm. The height z from the glass to the component surface and the working pressure are varied in the experiment, while the laser pulse of 20 ms at 6000 W remains constant. During the experiment, a shielding gas flow of argon 4.6 is supplied to the 95 l vacuum chamber, while the nominal cross-section of the vacuum pump and consequently the working pressure is regulated via a butterfly valve. The ZIROX XS22 32H-140 attached to the side of the vacuum chamber continuously measures the equalizing residual oxygen content. An exact measured composition of the atmosphere inside the chamber ist not carried out. The oxygen content within the tests of a pressure decade 10 mbar, 100 mbar and 1000 mbar was kept as constant as possible at XY, XY and XY repsectivley. After welding, the samples are stored directly in a desiccator to reduce further exposure of the particle deposits to the free atmosphere. For this study, stainless steel AISI 304 (also referred to as 1.4301 according to DIN EN 10027–2) with a material thickness of 4 mm and the dimensions of 60 mm × 80 mm is used as base material. To reduce measurement errors, each spot weld and deposit collection was carried out three times.

3. Results

3.1. Welding results and particle deposition

The deposits of the spot welds were collected on the glas carrier at heights z of 10 mm, 20 mm and 40 mm above the sample and at 10 mbar, 100 mbar and 1000 mbar working pressure. Thereby the significant difference between the working pressure are visible on the deposit at a height of 10 mm, which can be seen in Fig. 2 with the correlating spot welds. At working pressures of 10 mbar and 100 mbar, the resulting spot welds are almost identical. Only ther ring-shaped black deposit around the spot weld the 10 mbar in Fig. 2 a) are visually more pronounced compared to 100 mbar as shown in Fig. 2 c). Conversely, the dark black deposit on the glass carrier for 100 mbar appear stronger as seen in Fig. 2 d). The deposit on the glass carrier at 10 mbar indicates a strong thermal influence due to the flaking of the glass coating, see Fig. 2 b). In contrast, the deposits next to the spot weld and on the glass carrier at 1000 mbar, shown in Fig. 2 f) and f), are minimal with a slightly reddish coloration. An exact function which describes the density of the deposit in correlation with ambient pressure was not possible due to deviations through spatters and small segments of the glass coating.

3.2. REM & EDX analysis

First, the deposits on the glass carriers were examined with the SEM,

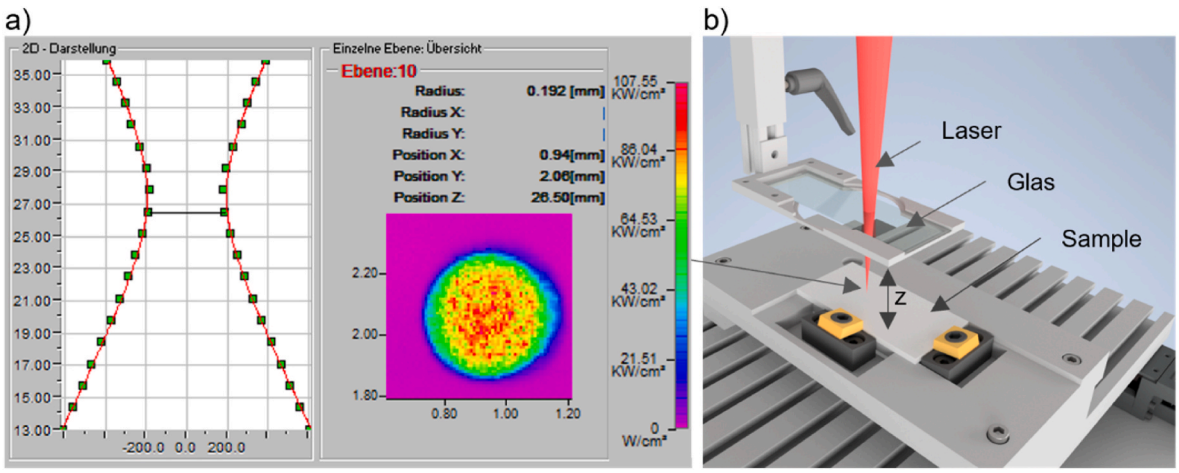


Fig. 1. a) Analyzed laser beam at 6000 W with intensity distribution in the focus plane b) Experimental setup for particle deposition on glass carrier with variable height z.

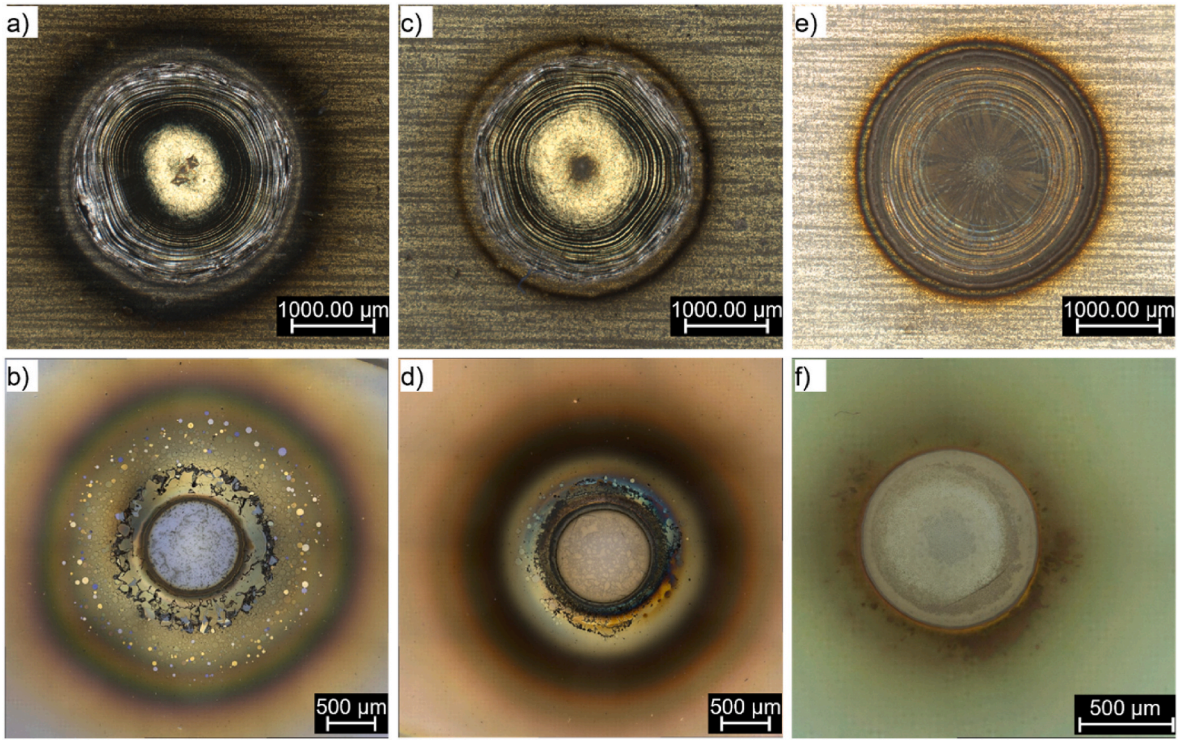


Fig. 2. Example of spot welds and corresponding depositions on glass carrier at a height of 10 mm from the process and at a)-b) 10 mbar c)-d) 100 mbar e)-f) 1000 mbar.

as shown in Fig. 3 a). The diameter of the laser beam d_{10}, which hits the glass carrier at a height of z = 10 mm, is around 940 µm in the beam measurement, see Table S1 in the Supporting Material section. As the thermal effect on the glass substrate is predominant in this range, the deposits are only observed from a distance r = 1.9 mm from the axis of the laser beam, as shown in the panoramic image Fig. 3 b). At a working pressure of 10 mbar and a height of 10 mm to the process, a cladding of the glass substrate with cracks can be seen 1.9 mm from the laser beam axis, see Fig. 3 c). This indicates that hot metal vapor is present and no particles are formed. Further away, r = 2.5 mm from the center, the cladding changes to a fine powder coating, which is then only purely powdery 3.2 mm away from the center.

If the height between the glass carrier and the welding process *z* is increased to 40 mm while the working pressure remains constant, no cladding of the glass carrier plate takes place near the laser axis, see Fig. 4 a). Instead, individual spherical particles adhering to each other can be seen, which form agglomerated particle clusters. These particle clusters decrease in number and size with the distance to the center of the laser axis, as can be seen in Fig. 4 b). The maximum magnification and image sharpness of the SEM images is limited by the non-conductive glass carrier plates and consequently the static charge, as well as by the relatively thin deposit.

The deposits on the glass carrier do not show complete plating over the analyzed area at 100 mbar and height z = 10 mm above the process. The surface structure of the deposits present nodular particle agglomerations adhering to each other, as shown in Fig. 5 a) at a distance of r = 2.5 mm from the center. With increasing height z to the process, this structure disappears and isolated cloud-like particle agglomerates are

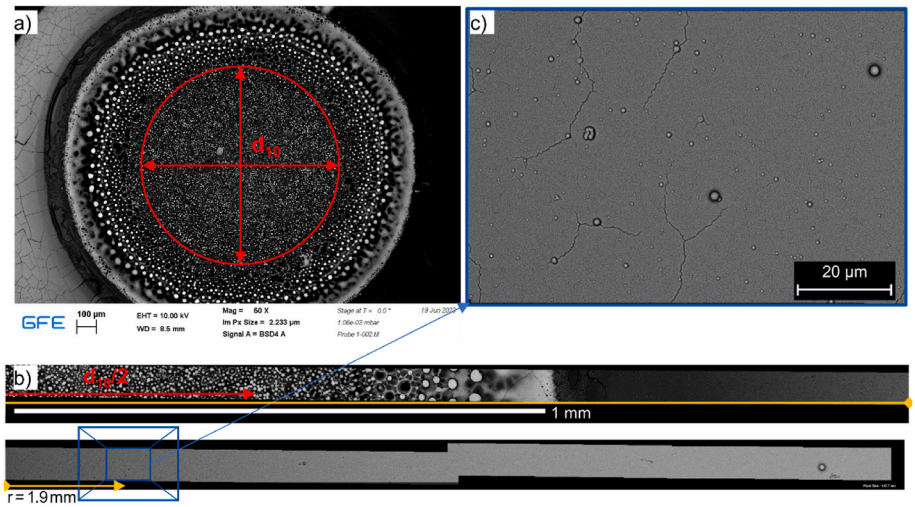


Fig. 3. a) SEM images of the deposits on glass carrier at a workting pressure of 10 mbar, a process height of 10 mm b) with corresponding panoramic image c) and close-up of the deposit 1.9 mm from the center of the laser axis.

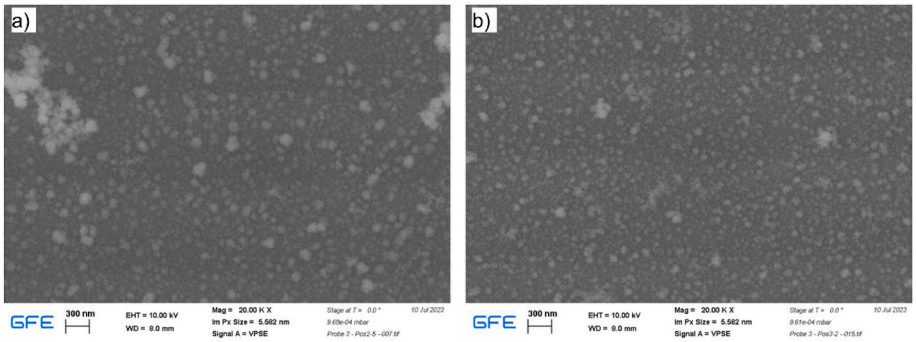


Fig. 4. SEM images of the deposits on glas carrier at a working pressure of 10 mbar, a process distance of 40 mm and a) 2.5 mm and b) 3.3 mm from the center oft he laser axis.

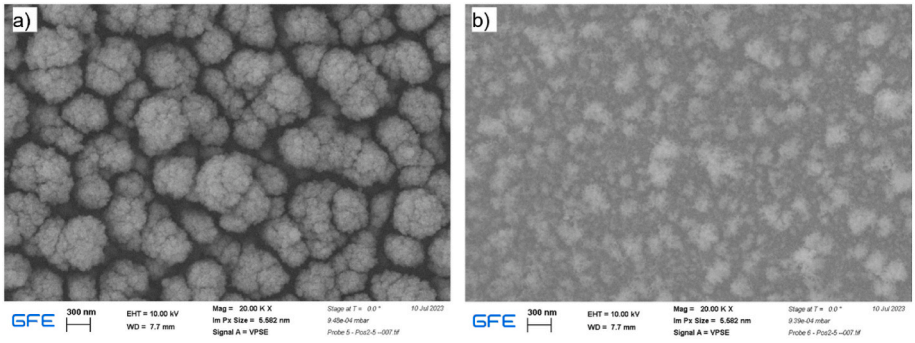


Fig. 5. SEM images of the deposits on glass carriers at a working pressure of 100 mbar and 2.5 mm from the center as well as a) 10 mm b) 20 mm process height.

deposited on the glass carriers, as shown in Fig. 5 b). At a height of 40 mm from the process, the deposits are so thin and finely distributed that no sharp structure can be analyzed with the SEM, as summarised in Fig. S1 in the Supporting Material section. The deposition 1.9 mm from the laser axis was not considered at this distance, as the glass carrier was again predominantly influenced by thermal effects.

At a working pressure of 1000 mbar, the nanoparticles are difficult to visualize on the SEM images, as shown in Fig. 6 a) for the distance of r = 2.5 mm from the center and a height of z = 10 mm from the process. The structure resembles a fine particle dust with isolated spherical nanoparticles. If only the process height is increased to 20 mm, smaller linked nanoparticles can be detected, Fig. 6 b. At a process height of 40 mm, the layer is again too thin to analyze the exact structure of the particles.

In order to analyze the deposits and the structure more clearly, the particles that are deposited next to the welds were also analyzed for all pressure decades. The metal background prevents static charging, which significantly increases the contrast. The SEM images for the three pressure decades 10 mbar, 100 mbar and 1000 mbar are shown in Fig. 7 a)-c). The deposits at 10 mbar show several smaller particles that have merged to a larger size, while at 100 mbar these larger sizes disappear and a nodular agglomeration of small nanoparticles can be detected. However, a further structural change in the deposit is clearly

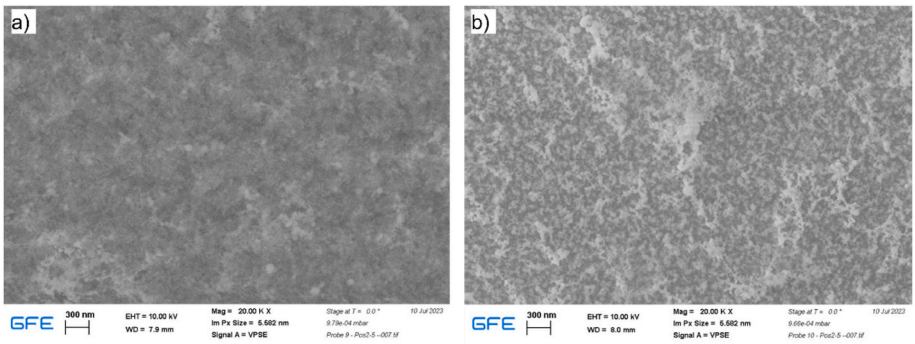


Fig. 6. SEM images of the deposits on glass carrier at a working pressure of 1000 mbar and 2.5 mm from the center as well as a) 10 mm b) 20 mm process height.

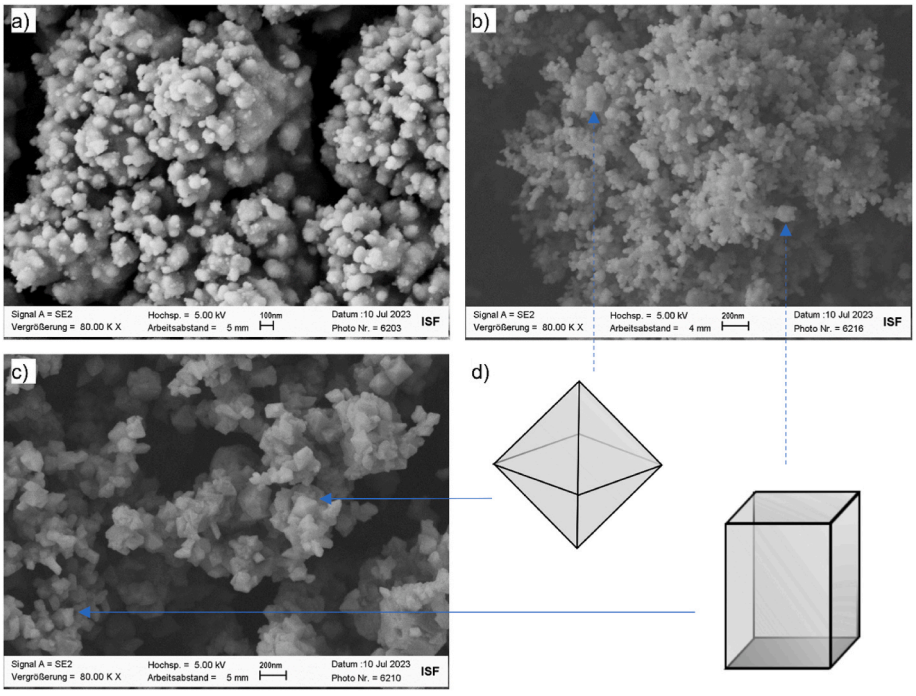


Fig. 7. Particle deposits next to the generated welding spots at a) 10 mbar b) 100 mbar c) 1000 mbar working pressure.

recognizable at 1000 mbar, in which the previously almost spherical particles show an agglomeration of prismatic and octahedron structures, Fig. 7 d). Occasionally, these prismatic, octahedral particle structures can also be assumed in the nodular agglomerations at 100 mbar.

The chemical composition of the deposits for the working pressures 10–1000 mbar from Fig. 7 are listed in Table 1 and show the published effect in Ref. [24] that the manganese content increases with decreasing pressure. This phenomenon is attributed to the fact that the element manganese has the lowest evaporation temperature of the investigated elements in the base material 304 (1.4301) and therefore changes to the vaporous aggregate state more quickly during the welding process than other elements such as iron or nickel [25]. In addition, it can be shown qualitatively that the oxygen content in the analyzed deposits correlates directly with reduced working pressure. The oxygen proportion of 43.04 at.% is higher than the iron proportion of 31.85 at.% at a working pressure of 1000 mbar while dropping to 1.28 at.% for 10 mbar. An exact quantitative measurement is not possible with the standardless SEM-EDX analysis used due to the low characteristic X-ray emission energy of oxygen.

3.3. TEM analysis

Deposited material from each of the three experiments was carefully ground in an agate mortar under ethanol and dispersed on holey carbon film-supported gold grids for subsequent analysis in the transmission electron microscope (FEI Tecnai G2 F20 S-TWIN) at 200 keV. For each

Table 1
Chemical composition of the deposits measured at four randomly chosen positons at different pressures (standardless SEM-EDX) in comparison to the base material (OES analyzation).

Pressure [mbar]	O [at.%]	Si [at.%]	Cr [at.%]	Mn [at.%]	Fe [at.%]	Ni [at.%]	Cu [at.%]
1000	43.04 ± 0.44	0.36 ± 0.01	13.97 ± 0.36	6.31 ± 0.14	31.85 ± 0.29	2.62 ± 0.12	1.87 ± 0.07
100	14.71 ± 0.51	0.41 ± 0.02	21.43 ± 0.16	17.25 ± 0.13	41.21 ± 0.33	2.33 ± 0.06	2.66 ± 0.05
10	1.28 ± 0.10	0.28 ± 0.04	23.48 ± 0.15	28.83 ± 0.13	42.17 ± 0.14	2.18 ± 0.02	1.77 ± 0.14
304 (1.4301)	–	0.67	19.40	1.51	70.18	7.84	0.39

stage, three regions on the grid with electron transparent agglomerates of particles were randomly chosen and analyzed by EDX and selected area electron diffraction (SAED). The particle agglomerates from the samples are shown in Fig. 8. To avoid presenting individual findings for the samples, the low resolution was selected to represent an integral. This established method is suitable for characterizing unknown ultrafine powders [26].

The results of the semi-quantitative (standardless) EDX analysis of the heavy elements for the three samples are summarised in Table S2 in the Supporting Material section. As all samples were inevitably contaminated by significant amounts of silicon oxide from grinding in the agate mortar, the latter elements were excluded from the evaluation of the EDX data.

Evaluation of the SAED patterns for phaseidentification was carried out using the FINDS software [27]. Reference data for the phases were in all cases reteived from the ICDD PDF5+ database [28]. Overlays of simulated electron diffraction ring patterns for comparison were created with the program RIPAS [29].

Visual inspection of the SAED patterns from the particles collected 10 mm above the process at 10 mbar and a residual oxygen value of 9300 ppm suggested a simple pattern which could then be readily indexed on the basis of a bcc lattice with an approximate lattice parameter of a ≈2.88 Å, see Fig. 9 a) and Fig. S2. A subsequent database search for the heavy elements detected by EDX within the expected error range yielded in total 57 matching phases, shown Table S3, indicating that the samples under investigation are a highly complex mixture of multiple bcc-type phases with varying chemical compositions. Since almost no reflections incompatible with the determined bcc lattice were detected, it can be concluded that the formation of metallic bcc particles is the dominant process under the lowest here investigated pressure conditions.

Analysis of the SAED patterns from the experiment carried out at 1000 mbar with a measured residual oxygen level in the vacuum chamber of 115,000 ppm, yields sets of completely different diffraction patterns with many reflections within the inner ring of the bcc pattern, see Fig. 9 c) and Fig. S4. The best matches found so far for this case, that cover nearly all observed reflection positions, are the spinel-type phases $NiCr_2O_4$ (PDF file #00-054-0961) and $NiFe_2O_4$ (PDF file #00-066-0245). The corresponding calculated ring patterns for both phases are shown as overlays in Fig. S5. Since the PDF5+ database lists several binary spinel phases AB_2O_4 with A = Cu, Cr, Fe, Mn, Ni and B = Cr, Fe, Ni, it is likely that these elements may also form a wide range of spinel-type solid solutions with highly variable chemical compositions and slightly different lattice parameters, similar to the ternary spinels $Cr_{0.5}Fe_{1.5}MnO_4$ (PDF file #01-089-3744), $Cu_{0.3}Fe_2Ni_{0.7}O_4$ (PDF file #01-084-6904) or $Cr_{0.03}Fe_{2.96}Ni_{0.01}O_4$ (PDF file #04-015-0675) under laser beam welding conditions at 1000 mbar of stainless steel. With regard to the results of the TEM-EDX analysis of the investigated particle agglomerates, the formation of pure Fe_3O_4 spinel as suggested initially, is very unlikely from the thermodynamic point of view, due to the higher entropy of the mixed spinels.

While the quest for the nature of the crystalline products at 10 mbar (bcc structure type) and 1000 mbar (spinel structure) could be satisfactorily answered, the patterns from the material obtained at 100 mbar with 16,000 ppm oxygen, shown Fig. 9 b) and Fig. S3, are more challenging. In addition to the reflections compatible with the bcc lattice, there are always several additional diffraction spots. However, the latter are not numerous enough to show a wide range of d-spacings of the contributing structure(s), making the commonly used fingerprint approach for phase identification highly unreliable. Nevertheless, it can be shown that almost all experimental reflections are compatible with those of the bcc and/or spinel pattern, so it is likely that the non-bcc reflections also originate from spinel-type crystallites formed at 100 mbar.

4. Discussion

4.1. Influence of glas carrier on welding results

The closer the glass particle carrier is to the process, the more particles are deposited and in turn influence the transmission of the laser radiation. As a result, some of the laser radiation is scattered and absorbed by the glass substrate, which explains the flaking of the coating and the burn-in. However, it can also be seen that with decreasing working pressure, the deposits tend to change to a coating similar to thermal spraying, whereas at atmospheric pressure and a height of 40 mm from the process, hardly any deposits can be found on the glass substrate. This can be explained by the fact that the formation of the metal vapor plume increases with decreasing pressure, as fewer molecules are available in the residual atmosphere for collision and cooling of the metal vapor plume [30]. Accordingly, the metal vapor in the vacuum and close to the process is hot enough to produce a coating on the glass substrate, while in the atmosphere the metal vapor has already cooled down to particles/particle agglomerates. If the vaporization or the number of particles on the glass carrier is sufficiently high, the laser radiation absorbs and scatters, which means that the glass can be more strongly affected by the laser pulse and the welding spot appears more pronounced. Quantitative measurement of the welding spots is therefore not useful in this study, but qualitative findings can be obtained. The effect that the welding depth increases with an increased oxygen value is already known and could also be determined in this study. Up to now, this increase in welding depth has been explained by the inward flow of molten pool currents that occur when the oxygen content is increased [31]. The extent to which the additional oxidation energy from the oxygen influences this increase in depth has not been considered yet. It is conceivable that the exothermic oxidation reaction adds additional

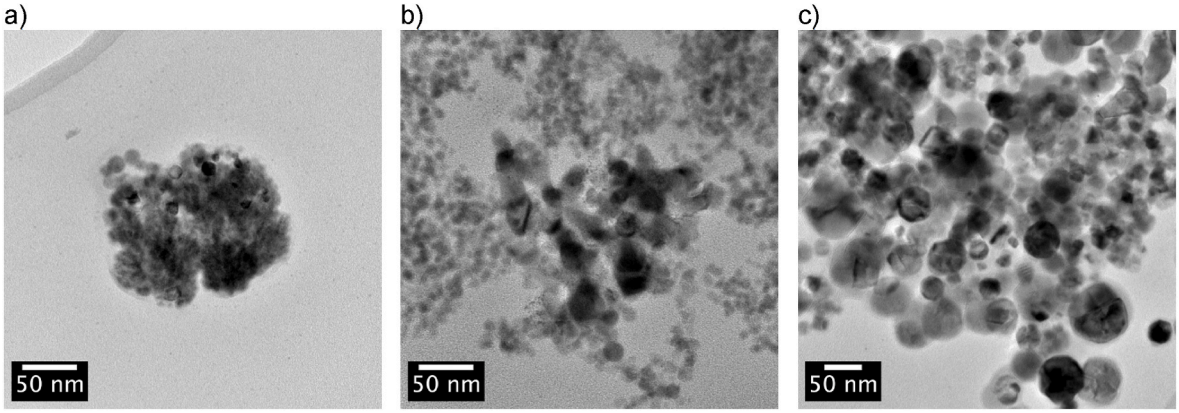


Fig. 8. Typical STEM images of particle agglomerates from the samples at a) 10 mbar, b) 100 mbar, and c) 1000 mbar.

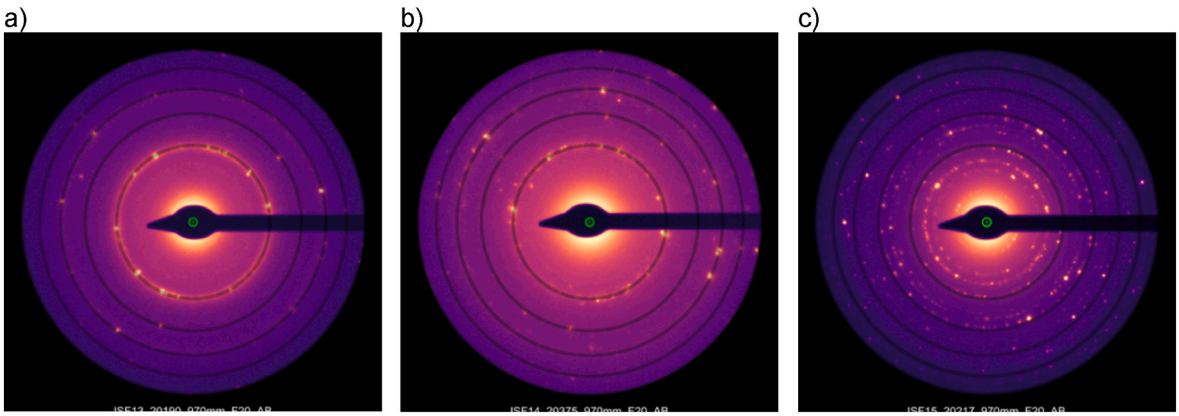


Fig. 9. Typical electron diffraction patterns from the samples obtained from laser beam welding under a) 10 mbar, b) 100 mbar and c) 1000 mbar with overlayed rings marking the ideal positions of bcc lattice reflections of a = 2.88 Å (for more details see Figs. S2–S4).

energy to the melt pool and thereby changes the melt pool flow. Another explanation is that the oxidation of particles reduces the scattering and absorption of the laser beam and consequently more energy reaches the capillary.

4.2. Metal vapor composition

As can be seen in the deposits on the glass carrier in SEM images, a structural change takes place depending on the pressure component, whereby a color change of the deposits from red to black is visually perceptible. This can be partly explained by the more pronounced metal vapor content with decreasing pressure, whereby the deposits near the process tend to be accompanied by a coating and further away the particles coalesce into agglomerates. These resulting nodular agglomerates at 100 mbar take on nanostructures that strongly absorb the incident light, which explains the perceptible black color of the deposit. This effect also occurred with laser structuring of gold surfaces, in which the deposits take on almost identical structures: „The examination of the black halo produced around the crater shows that its elemental composition […] is identical to that for a pristine surface, i.e., the black halo is a layer of the ablated and redeposited gold" [32]. As a result, the absorption of the femtosecond laser varies in the study, as the surface structure changes due to the deposits and consequently more power is absorbed in an uncontrolled manner. It was not possible to determine whether this deposit structure forms in the air or only when it hits the component.

At 1000 mbar, the EDX analysis shows a significantly increased oxygen content in the deposits and more octahedral particles in the SEM images, which are also occasionally visible at 100 mbar. These particles were assigned at first sight to spinel-type Fe_3O_4 by comparing the SEM images of the oxides structure [22]. However, the TEM analyses identifies much more complex phases, that are structurally related to Fe_3O_4 and show diffraction patterns compatible with spinel-type $NiCr_2O_4$ and $NiFe_2O_4$. In addition, the characteristic octahectral and cubic structures, which are already visible in the SEM images, are recognizable in the STEM images. Whether there are also the assumed different Fe_3O_4 phases or more likely several spinel phases of AB_2O_4 with A = Cu, Cr, Fe, Mn, Ni and B = Cr, Fe, Ni cannot be made on the basis of diffraction data due to the ambiguity [33]. Therefore, electron energy loss spectroscopy (EELS) can be used to distinguish between the particles. However, the results for sum spectra of particle clusters are also ambiguous in some cases. If multiphase nanopowders with different iron contents are also present, the measurement results are further distorted. Furthermore, residual gas contamination inside the vacuum chamber can influence the particle synthesis, which should be considered in further investigation. The Fe_2O_3 (hematite) initially suspected due to the reddish coloration of the deposits is not evident in the measurement data.

4.3. Theoretical influence of oxygen

The EDX analysis of the deposit next to the welding position presents a decreasing oxygen content while the portion of pure iron slightly increases. In the assumption that all measured oxygen is used for building iron-oxide, the theoretical portion of the measured iron on Fe_3O_4 is 100 % at 1000 mbar, 27 % at 100 mbar and 2 % at 10 mbar, as shown in Fig. 10. This consideration is based on the fact that three-sevenths of iron atoms and four-sevenths of oxygen atoms are required for one iron oxide Fe_3O_4. Accordingly, when welding in the atmosphere, the oxygen would bind all the iron particles, resulting in an Fe_3O_4 content of 75.32 at.% in the total deposition. Consequently, a distinction must be made in the assumptions for multi-wavelength methode or calculating the extinction of the laser in process simulations as to whether pure iron particles or iron oxide particles are present. However, this applies explicitly to pure iron and neglecting the other alloying elements present in stainless steel. In addition to Fe_3O_4, FeO phases and other suboxides could also form in a vacuum with insufficient oxygen, which are not considered.

It should be noted that the formation of iron oxides is associated with the oxygen content present in the vacuum. However, this was only measured and not explicitly varied, which is why we refer to the pressure. The molar density of oxygen in the 95 l vacuum chamber measures 4.72 mol/m³, $0.66*10^{-1}$ mol/m³, $0.38*10^{-2}$ mol/m³ for 1000 mbar, 100 mbar, 10 mbar, respectively. Therefore, more oxygen molecules are available to bind the iron molecules inside the metal vapor. In addition, the standard enthalpy of formation for iron oxide Fe_3O_4 is $\Delta_f H^o_{solid}$ =

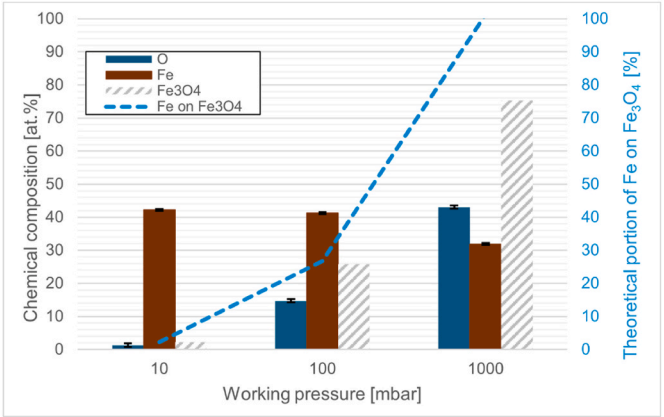


Fig. 10. Theoretical portion of measured Fe atoms on Fe_3O_4 (right scale) and total Fe_3O_4 over working pressure based on measured chemical composition of the deposition (left scale).

−1120.89 kJ/mol [34], which enhances the local energy in the metal vapor plume. This oxidation energy heats up the metal vapor plume, which results in more detectable thermal emissions [35] and changes in melt pool geometry [36]. These changes can be attributed to the altered marangoni flows, which at the same time cause an increased welding depth with a higher oxygen content inside the vacuum chamber [21]. Besides, a higher oxygen content in atmosphere or shielding gas, leads to homogenization of chromium and nickel inside the weld which affect the microstructure of the weld seam [37]. Therefore, it is of great importance for future investigations to consider not only the pressure in the vacuum chamber, but also the exact composition of the contained atmosphere as well as oxygen-, hydrogen- and nitrogen-content of the base material as shown in Table S4 in the Supporting Material.

5. Conclusions

The study shows that the shape, structure and chemical composition of the metal vapor plume is highly complex and changes in axial and radial directions depending on the working pressure. The hot metal vapor plume reaches higher at 10 mbar and still provides a smooth coating at 20 mm above the process while forming small bcc-type particles containing Cr, Cu, Fe, Mn and Ni. In contrast, at 1000 mbar complex spinel-type phases with cubic lattice structure are formed at 10 mm above the process. The formation of pure Fe_3O_4 spinel as suggested initially, is very unlikely, rather several spinel-type solid solutions with the alloying elements Cu, Cr, Fe, Mn, Ni from the base material 304 (1.4301). The working pressure in between of 100 mbar forms a deposit of characteristic nodular structures that are known to increase the absorption of laser radiation from nanostructuring. Additionally, a mixture of bcc-type and spinel-type particles are present in the TEM analysis.

Theoretical considerations show that in atmospheric welding the particle composition consists with around 75 at.% mainly of Fe_3O_4 particles with the assumption all iron atoms react with oxygen, while at reduced pressure or reduced oxygen content, particles of pure iron are produced for the most part. However, this theory does not consider further chemical elements of the steel alloy, whereby it applies most likely to welding pure iron in a controlled vacuum environment.

The complexity of the composition, geometric shape and topography of the particles in the metal vapor plume during laser beam welding in a vacuum has been revealed and will help in future studies to determine the particle size using the multi-wavelength method or calculate the scattered laser light in process simulations.

CRediT authorship contribution statement

Christian Frey: Writing – review & editing, Writing – original draft, Visualization, Validation, Methodology, Investigation, Data curation, Conceptualization. **Johannes Wahl:** Writing – review & editing, Investigation. **Kathrin Schmidt:** Writing – review & editing, Investigation. **Simon Olschok:** Supervision, Conceptualization. **Christian Hagenlocher:** Writing – review & editing, Supervision, Conceptualization. **Thomas E. Weirich:** Writing – review & editing, Validation, Investigation, Data curation. **Thomas Graf:** Project administration, Funding acquisition. **Uwe Reisgen:** Project administration, Funding acquisition.

Data availability statement

Supporting Material are available in a separate file attached. The additional raw data that support the findings of this study are available from the corresponding author under the following link and upon reasonable request: http://hdl.handle.net/21.11102/1f8d7257-b478-440e-9b92-317a732dccf8.

Declaration of competing interest

We declare that we have no financial and personal relationships with other people or organizations that can inappropriately influence our work, there is no professional or other personal interest of any nature or kind in any product, service and/or company that could be construed as influencing the position presented in, or the review of, the manuscript entitled.

Acknowledgements

The presented work was funded by the Deutsche Forschungsgemeinschaft (DFG, German Research Fundation) – Project number 463452146. Furthermore, we thank C. Herwartz, Dr. A. Schwedt, R. Harscheidt and F. Mariano at the Central Facility for Electron Microscopy (GFE), who performed the TEM and SEM investigations.

Appendix A. Supplementary data

Supplementary data to this article can be found online at https://doi.org/10.1016/j.vacuum.2024.113964.

Data availability

Data will be available under shared link and reasonable request.

References

[1] Y. Arata, N. Abe, T. Oda, N. Tsujii, Fundamental phenomena during vacuum laser welding, in: Laser Institut of America, Editor. International Congress on Applications of Lasers & Electro-Optics//Proceedings of the Materials Processing Symposium: ICALEO ' 84, Laser Institute of America, 1984, pp. 1–7.
[2] M. Jiang, W. Tao, Y. Chen, Laser welding under vacuum: a review, Appl. Sci. 7 (9) (2017) 909, https://doi.org/10.3390/app7090909.
[3] P. Shcheglov, Study of vapour-plasma plume during high power fiber laser beam influence on metals. Bundesanstalt für Materialforschung und -prüfung (BAM), Zugl.: Moskow, National Research Nuclear Univ., Diss., Berlin, 2012, 2012.
[4] D.F. Farson, K.R. Kim, Generation of optical and acoustic emissions in laser weld plumes, J. Appl. Phys. 85 (3) (1999) 1329–1336, https://doi.org/10.1063/1.369263.
[5] T. Scholz, Nanopartikelbildung beim Laserschweißen von Metallen [Dissertation], Ruhr-Universität Bochum, Bochum, 2015.
[6] Z. Szymański, J. Kurzyna, Spectroscopic measurements of laser induced plasma during welding with CO2 laser, J. Appl. Phys. 76 (12) (1994) 7750–7756, https://doi.org/10.1063/1.357952.
[7] M. Schellhorn, CO-Hochleistungslaser: Charakteristika und Einsatzmöglichkeiten beim Schweissen, second ed., Utz, München, 2005.
[8] S. Hwan Lee, J. Mazumder, Characteristics of disk laser-induced plasma. In: laser Institut of America, in: 4th Pacific International Conference on Laser Materials Processing, Micro, Nano and Ultrafast Fabrication vol. 32826, Laser Institute of America, Orlando, FL, 2010, pp. 33–38.
[9] S.A. Uspenskiy, V.N. Petrovskiy, D.P. Bykovskiy, v. d. Mironov, N.M. Prokopova, E. V. Tret'yakov, Spectral diagnostics of a vapor-plasma plume produced during welding titanium with a high-power ytterbium fiber laser. 23rd International Laser Physics Workshop (LPHYS'14), IOP Publishing Ltd, 2015.
[10] Johannes Wahl, Christian Frey, John Powell, Felix Zaiß, Michael Haas, Simon Olschok, Uwe Reisgen, Christian Hagenlocher, Thomas Graf, Laser-plume interactions in deep-penetration remote laser welding of stainless steel, J.: Laser. Manufact. Mater. Process. (2024) (In Review).
[11] A.G. Gnedovets, A.V. Gusarov, I. Smurov, G. Flamant, Hydrodynamics of laser erosive jet generating nanoscale particles, Appl. Surf. Sci. 109–110 (1997) 74–79, https://doi.org/10.1016/S0169-4332(96)00738-6.
[12] A. Matsunawa, S. Katayama, A. Susuki, T. Ariyasu, Laser production of metallic ultra-fine particles, Transac. Japan Weld. Res. Ins. 15 (2) (1986) 61–72.
[13] A. Michalowski, A. Heß, A. Ruß, F. Dausinger, Plume attenuation under high power Yb:YAG laser material processing, in: Wissenschaftliche Gesellschaft Lasertechnik (Ed.), Proceedings of the Fourth International WLT-Conference on Lasers in Manufacturing 2007, 2007, pp. 357–362.
[14] R. Fabbro, S. Slimani, I. Doudet, F. Coste, F. Briand, Experimental study of the dynamical coupling between the induced vapour plume and the melt pool for Nd–Yag CW laser welding, J. Phys. Appl. Phys. (39) (2006) 394–400, https://doi.org/10.1088/0022-3727/39/2/023.
[15] F. Kaufmann, J. Ermer, A. Maier, S. Roth, M. Schmidt, Influence of plume attenuation under high power laser welding of copper using visible wavelengths, J. Laser Appl. 33 (4) (2021) 1–9, https://doi.org/10.2351/7.0000505.

[16] G. Mie, Beiträge zur Optik trüber Medien, speziell kolloidaler Metallösungen, Ann. Phys. 330 (3) (1908) 377–445, https://doi.org/10.1002/andp.19083300302.
[17] K. Schaber, A. Schenkel, R. Zahoransky, Drei-Wellenlängen-Extinktionsverfahren zur Charakterisierung von Aerosolen unter industriellen Bedingungen, Techhnisches Messen 61 (7/8) (1994) 295–300, https://doi.org/10.1524/teme.1994.61.jg.295. JG)).
[18] J. Greses, P.A. Hilton, C.Y. Barlow, W.M. Steen, Plume attenuation under high power Nd:YAG laser welding, in: The Laser Institute of America, Editor. 21st International Congress on Applications of Lasers & Electro-Optics vol. 32826, Laser Institute of America, Orlando, FL, 2002.
[19] D. Lacroix, G. Jeandel, C. Boudot, Solution of the radiative transfer equation in an absorbing and scattering Nd:YAG laser-induced plume, J. Appl. Phys. 84 (5) (1998) 2443–2449, https://doi.org/10.1063/1.368405.
[20] T. Scholz, K. Dickmann, A. Ostendorf, Investigation of the formation of nanoparticles during laser remote welding, in: C. Emmelmann, M.F. Zaeh, T. Graf, M. Schmidt (Eds.), Lasers in Manufacturing 2013: Proceedings of the 7ifth International WLT-Conference Lasers in Manufacturing, 2013, pp. 90–97. Munich, Germany, Mai [13th - 16th] 2013.
[21] T. Twiehaus, S. Olschok, U. Reisgen, Influence of residual oxygen during laser beam welding under vacuum, Mater. Test. 64 (7) (2022) 945–953, https://doi.org/10.1515/mt-2021-2183.
[22] R.M. Cornell, U. Schwertmann, The Iron Oxides: Structure, Properties, Reactions, Occurrences, and Uses, second ed., Wiley-VCH, Weinheim, 2003.
[23] C. Stötzel, H.-D. Kurland, J. Grabow, S. Dutz, E. Müller, M. Sierka, et al., Control of the crystal phase composition of Fe x O y nanopowders prepared by CO 2 laser vaporization, Cryst. Growth Des. 13 (11) (2013) 4868–4876, https://doi.org/10.1021/cg4010533.
[24] T. Twiehaus, Optimierung des Laserstrahlschweißens im Vakuum zu einem hochqualitativen Schweißverfahren für nichtrostende Stähle und Refraktärmetalle [Dissertation]. Aachen, RWTH Aachen University, 2023.
[25] R.E. Honig, D.A. Krammer, Vapor data pressure for the solid and the liquid elements, RCA Rev. (30) (1969) 285–305.
[26] C.E. Lyman, M.J. Carr, Lndentification of Unknowns, in: M. Cowley J (Ed.), Electron Diffraction Techniques, Oxford University PressOxford, 1993, pp. 373–418.
[27] T.E. Weirich, FINDS: an ImageJ script for rapid non-matrix diffraction spot identification in selected area electron diffraction patterns, Powder Diffr. (2024) 1–8, https://doi.org/10.1017/S0885715624000538. Published online.
[28] S.N. Kabekkodu, A. Dosen, T.N. Blanton, PDF-5+: a comprehensive Powder Diffraction File™ for materials characterization, Powder Diffr. 39 (2) (2024) 47–59, https://doi.org/10.1017/S0885715624000150.
[29] T.E. Weirich, RIPAS: Eine minimalistische Desktop-Anwendung zur Simulation von Elektronenpulverdiffraktogrammen, RWTH Aachen University, 2023.
[30] C. Frey, S. Olschok, U. Reisgen, M. Sawannia, R. Weber, Proof of concept to analyze process emissions during laser beam welding at different ambient pressures, Procedia CIRP 111 (2022) 547–550, https://doi.org/10.1016/j.procir.2022.08.145.
[31] C.X. Zhao, C. Kwakernaak, Y. Pan, I.M. Richardson, Z. Saldi, S. Kenjeres, et al., The effect of oxygen on transitional Marangoni flow in laser spot welding, Acta Mater. 58 (19) (2010) 6345–6357, https://doi.org/10.1016/j.actamat.2010.07.056.
[32] A.Y. Vorobyev, C. Guo, Enhanced absorptance of gold following multipulse femtosecond laser ablation, Phys. Rev. B 72 (19) (2005), https://doi.org/10.1103/PhysRevB.72.195422.
[33] I. Slabu, N. Wirch, T. Caumanns, R. Theissmann, M. Krüger, T. Schmitz-Rode, et al., Electron tomography and nano-diffraction enabling the investigation of individual magnetic nanoparticles inside fibers of MR visible implants, J. Phys. D Appl. Phys. 50 (31) (2017) 315303, https://doi.org/10.1088/1361-6463/aa77e8.
[34] W. Malcolm, JR. Chase, NIST-JANAF thermochemical tables fourth edition Part I, Al-Co, J. Phys. Chem. Ref. Data Monograph No. 9 (1998) 1–61.
[35] C. Frey, A. Beyel, J. Wahl, T. Twiehaus, S. Olschok, C. Hagenlocher, et al., Interdependence of metal vapor plume and melt pool dynamics during laser beam welding under vacuum, J. Laser Appl. 36 (4) (2024) 1–10, https://doi.org/10.2351/7.0001557.
[36] F. Yang, X. Meng, S.N. Putra, A. Artinov, M. Bachmann, M. Rethmeier, Numerical analysis of the effect of an oscillating metal vapor plume on the keyhole and molten pool behavior during deep penetration laser beam welding, J. Laser Appl. 35 (4) (2023) 1–9, https://doi.org/10.2351/7.0001094.
[37] S. Li, Z. Zhou, G. Xiao, B. Chen, Influence of carbon dioxide shielding gas on microstructure and corrosion property of welds, Mater. Werkst. 50 (7) (2019) 819–828, https://doi.org/10.1002/mawe.201800129.